

Article

Relative Humidity Measurement Based on a Tapered, PVA-Coated Fiber Optics Multimode Interference Sensor

Abraham A. Quiñones-Flores ^{1,*}, Jose R. Guzman-Sepulveda ²  and Arturo A. Castillo-Guzman ¹ 

¹ Facultad de Ciencias Físico Matemáticas, Universidad Autónoma de Nuevo León, San Nicolás de los Garza 66455, Nuevo León, Mexico; arturo.castillogz@uanl.edu.mx

² Centro de Investigación y de Estudios Avanzados del IPN, Unidad Monterrey, Vía del Conocimiento 201, Parque de Investigación e Innovación Tecnológica, km 9.5 de la Autopista Nueva al Aeropuerto, Apodaca 66600, Nuevo León, Mexico; jose.guzmans@cinvestav.mx

* Correspondence: abraham.quinonesfl@uanl.edu.mx

Abstract: A relative humidity (RH) fiber optic sensor is demonstrated based on the multimode interference (MMI) phenomenon utilizing a no-core fiber (NCF) coated with polyvinyl alcohol (PVA). The sensor's structure is simple and consists of a section of NCF spliced between two standard single-mode fibers (SMFs). The fabrication and testing of a tapered version with enhanced sensitivity is also presented. The native MMI sensor showed a sensitivity of 5.6nm/RH%, in the range from 87 RH% to 93 RH%, while the tapered one exhibited an increased sensitivity of 6.6nm/RH%, in the range from 91.5 RH% to 94 RH%. The sensitivity values obtained with these MMI sensors are at least twice as large as the most sensitive fiber optics humidity sensor reported in the literature in a similar RH range.

Keywords: fiber sensor; multimode interference; optic fiber taper; no core fiber; relative humidity



Citation: Quiñones-Flores, A.A.; Guzman-Sepulveda, J.R.; Castillo-Guzman, A.A. Relative Humidity Measurement Based on a Tapered, PVA-Coated Fiber Optics Multimode Interference Sensor. *Optics* **2023**, *4*, 473–481. <https://doi.org/10.3390/opt4030034>

Academic Editor: Francesco Chiavaioli

Received: 19 June 2023

Revised: 18 July 2023

Accepted: 26 July 2023

Published: 31 July 2023



Copyright: © 2023 by the authors. Licensee MDPI, Basel, Switzerland. This article is an open access article distributed under the terms and conditions of the Creative Commons Attribution (CC BY) license (<https://creativecommons.org/licenses/by/4.0/>).

1. Introduction

Optical fibers have been extensively used for the fabrication of sensors for various physical and chemical variables, especially due to their advantageous characteristics of immunity to electromagnetic perturbations, resistance to corrosion, compactness, cost-effectiveness, stability in hostile environments, and the capability for remote monitoring [1,2]. Among the different variables, humidity has been of interest not only for its implications in meteorology and human comfort, e.g., air conditioning and intelligent control of living environments, but also because of the critical role it plays in a variety of industrial settings, including biomedical, e.g., respiratory equipment, sterilizers, and incubators; electronics, e.g., semiconductor wafer processing; and, agricultural, e.g., plantation protection and soil moisture monitoring, among many others [3]. Over the years, humidity sensing has been a challenging, active area that encourages simultaneously the development of both new sensing strategies and new materials that can work as transducers for humidity [4,5]. In this regard, optical sensing schemes have been demonstrated to be a suitable approach [6] and, in particular, those based on optical fiber technology are attractive due to the characteristics mentioned above [7,8].

Out of all the metrics used to measure humidity, relative humidity (RH) is the most popular, especially because its definition, interpretation, and usage are straightforward. RH describes the relation between the water vapor pressure present in the air and the saturation water pressure at a specific temperature. This is meant to say that RH describes the percentage of water vapor in the air relative to the maximum amount of water vapor that air can hold at a given temperature. Sensing RH with optical waveguides has been achieved by incorporating special materials that respond to changes in RH into various types of optical fiber-based sensing schemes. For example, polyvinyl alcohol (PVA) is a

bio-compatible substance, soluble in water, that has been used successfully for RH fiber optic sensors [9,10].

In addition, the already outstanding sensing capabilities of optical fibers can be enhanced further by tapering them in order to induce stronger evanescent interactions [11–13]. Moreover, the multimodal interference (MMI) phenomenon in optical fibers has been thoroughly studied, giving rise to many photonic devices, particularly fiber optic sensors [14–19] and lasers [20]. Furthermore, many RH sensors have been developed based on the MMI effect due to their simplicity, ease of assembly, low-cost requirement, and dexterity to set up non-conventional sensing schemes. A few notable examples are those in Ref. [21], where the authors made a simple RH sensor using an etched multimode fiber (MMF) coated with PVA with a sensibility of 0.09 nm/RH%, and in Ref. [22], where the authors used a photonic crystal fiber as the multimode section of the MMI covered in polyallylamine hydrochloride (PAH) and polyacrylic acid.

In this study, we have assembled two similar RH optic fiber sensors based on the MMI effect. These sensors' multimode sections are coated with PVA as the RH-sensitive material. A specialty fiber known as no core fiber (NCF) was used as the multimode component of our fiber structures due to its increased sensitivity for evanescent wave-sensing applications [18]. The NCF section of the second sensor was tapered at the center using a fusion splicer. In this regard, it has also been noticed that tapering the multimode section in an MMI fiber optics device helps to increase the sensitivity [19]. Both RH sensors based on the MMI effect using PVA-coated NCF have a high sensitivity, at least twice as large as the most sensitive fiber optics sensors reported in the literature.

2. Materials and Methods

2.1. Multimode Interference (MMI) Principle and Device Fabrication

The base for our RH optic fiber sensors is an MMI device whose structure consists of a section of NCF spliced between two standard single-mode fibers (SMFs), as illustrated in Figure 1. This structure will be referred to as SMF-NCF-SMF throughout this work. The MMI device acts as a spectral filter governed by the following equation:

$$\lambda_{peak} = p \frac{n_{eff} D_{eff}^2}{L}, \quad (1)$$

where λ_{peak} is the wavelength at which the characteristic filter-like spectral response of the MMI device has its peak; p is the so-called self-imaging index; n_{eff} and D_{eff} are the effective refractive index (RI) and the effective optical diameter of the multimode section, respectively; and, L is the length of the NCF. When $p = 4$, the input spectrum is completely reconstructed at the NCF-SMF interface. The effective diameter that appears in Equation (1) can be approximated to:

$$D_{eff} = D + \frac{\lambda}{2\pi} (n_{NCF}^2 - n_m^2)^{-\frac{1}{2}} \left(\frac{n_{NCF}^2}{n_m^2} + 1 \right), \quad (2)$$

where D is the physical diameter of the NCF, and the second term reflects the evanescent penetration into the cladding, where n_{NCF} is the RI of the core of the multimode section (of the NCF in our case), and n_m is the RI of the medium surrounding the NCF, which plays the role of its cladding. When working with increasingly smaller NCF diameters, the second term of Equation (2) has more influence on the value of D_{eff} . Given the previous fact, it can now be seen that the smaller the physical diameter of the NCF is, the more impact on λ_{peak} the refractive indices of the NCF and the medium surrounding it will have.

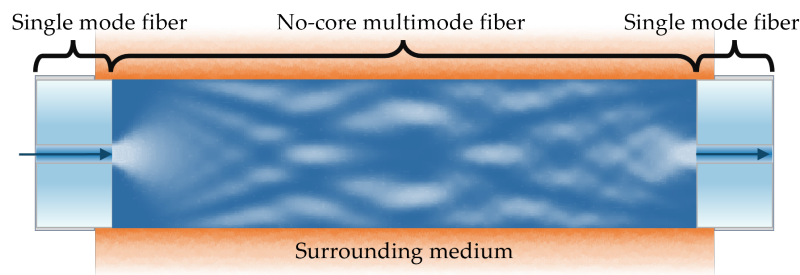


Figure 1. NCF MMI structure used as the base for the sensor.

To build the fiber structure using a fusion splicer, an SMF was spliced to an NCF with a diameter of 125 μm . Next, the NCF was measured to a length of $L = 59$ mm and cleaved. The length of the NCF was chosen to have the 4th image at a wavelength of 1550 nm. Thus far, we have an SMF spliced to a 59 mm long NCF. Finally, the end of the NCF was spliced to the output SMF. An integrated broadband light source ranging from 1450 nm to 1630 nm with peak power at 1550 nm from an optical spectrum analyzer (OSA) was used to illuminate our fiber structures. The original spectrum and the resulting spectrum from transmitting the original through the MMI device are shown in Figure 2.

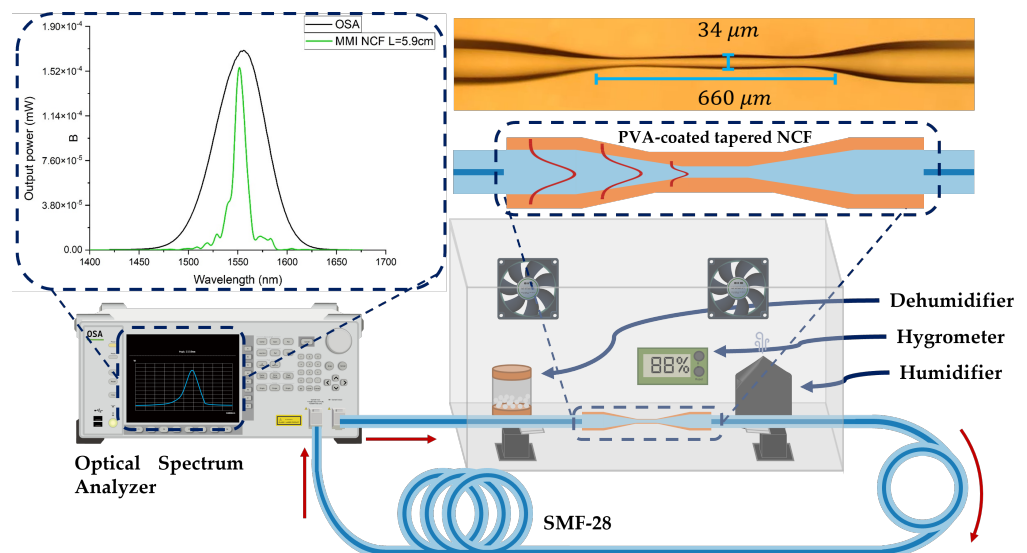


Figure 2. Sketch of the experimental setup and an image of the tapered NCF.

Regarding the sensor fabrication, it should be noted that the most critical aspect is having the section of NCF with the right length (estimated from Equation (1)). To achieve this, we followed a simple procedure which consists in splicing the SMF to the NCF; then, the desired length of NCF is measured with a general purpose vernier caliper, taking the splice as the zero length, while keeping the NCF straight; then, the NCF is marked at the desired length and cleaved at the mark; finally, the second SMF is spliced. By performing a simple variational analysis of Equation (1), one can see that the variation in λ_{peak} produced by an error in the length of the NCF, is $\delta\lambda_{peak} = \left(\frac{\partial\lambda_{peak}}{\partial L}\right)\delta L = -\left(p\frac{n_{eff}^2 W_{eff}^2}{L^2}\right)\delta L$. Thus, by taking $p = 4$, $n_{eff} \approx 1.444$, $W_{eff} \approx 125$ μm , $L = 59$ mm, and considering the resolution of the vernier caliper as $\delta L = 0.05$ mm, the error in the peak wavelength is of $\delta\lambda_{peak} \approx 1.3$ nm. This simple procedure is robust enough to engineer MMI sensing architectures where multiple sensors operate simultaneously, each of them in its own spectral window but all of them within the range of a single broadband light source [23].

A fusion splicer was used for its fabrication once the MMI device was constructed. The tapering process was performed manually by applying an electric discharge on the fiber while keeping it under tensile stress; the fiber was stretched controllably by using

the stepper motors of the splicer. This process was performed multiple times in sequence (not necessarily with the same parameters each time) until the desired taper was achieved. For the tapers fabricated with the same recipe, the variability of the waist diameter and the variability of the taper's length is around 4% and 6%, respectively, with respect to the target dimensions thus allowing for the consistent production of tapered MMI sensors.

2.2. PVA Coating

The NCF section of the assembled fiber structure was coated with PVA. The PVA coating was prepared by adding 10 g of dry PVA powder into 100 mL of water and mixed at 90 °C for an hour using a magnetic mixer, resulting in a viscous, fully transparent PVA-water liquid mixture. Next, a small amount of the previously prepared PVA mixture was poured into a clock glass, and the NCF section of the SMF-NCF-SMF structure was completely submerged into the PVA mixture for 10 s. Immediately after, while slightly applying tension, the fiber structure was strummed once. Due to the previous action, the excess PVA was removed by the induced vibration of the fiber. Finally, the PVA-coated fiber was set to dry for at least two hours at ambient conditions. This procedure was repeated in the same way for the tapered NCF.

In our configuration, the MMI device responds to the refractive index (RI) of the medium surrounding the NCF due to the evanescent interaction that takes place due to the fact that the NCF does not have a cladding; in other words, the PVA coating plays the role of the cladding of the NCF. Importantly, the evanescent field traveling outside the NCF and interacting with the PVA coating extends a very short distance beyond the surface of the NCF, typically on the order of the wavelength. If the coating is thicker than the extent of the evanescent field, the sensitivity should not depend on its thickness. In fact, the second term in Equation (2) represents the evanescent penetration of the light into the cladding, providing a small correction on the geometrical diameter of the NCF to estimate the effective optical diameter, D_{eff} . By taking the RI of the PVA coating as $n_m \approx 1.40$ [24], the extent of the evanescent field is 1.4 μm , which is approximately one wavelength; as long as the PVA coating is thicker than that, the sensor's sensitivity does not depend on the thickness. Even though the diameter of the coated fibers shows some variability from sample to sample, we note that the variability of the diameter along a single coated fiber is smaller than 10% with respect to the average value. Moreover, the minimum thickness of the PVA coating obtained in this study was 14 μm , which is much larger than the reach of the evanescent field; in other words, the evanescent field remains well within the PVA coating at all times.

3. Results

For the non-tapered structure, there was little to no change in the recorded transmission spectrum in the range from 40%RH to 86%RH. Once the RH in the enclosure reached 87%, a noticeable shift in peak wavelength to the left was recorded, going from 1603 nm at 87%RH to 1570 nm at 93%RH. The spectra shown in Figure 3 were recorded at integer values of %RH. As mentioned, there is a significant blue-shift behavior as the humidity increases. The optical power increase is seen as %RH increased, but this behavior is due solely to the shape of the used light source, as seen in Figure 2. As the peak wavelength shifts closer to 1550 nm, it increases in optical power. The plot of peak wavelength concerning %RH is also shown in Figure 3, revealing a highly linear dependence with a sensitivity of 5.6nm/%RH, as indicated.

Similarly, for the case of the tapered sensor, minimal variations in the optical spectrum were observed from 40%RH to 92%RH. After that, a blue shift in the peak wavelength was recorded, as indicated in Figure 4, going from 1512 nm at 92.5%RH to 1501.5 nm at 94%RH. Following the shift of the peaks at the center of the spectrum, a sensitivity of 6.6 nm/%RH can be estimated, as indicated. The MMI sensor with the tapered NCF showed an increase in the sensitivity as compared to the non-tapered one.

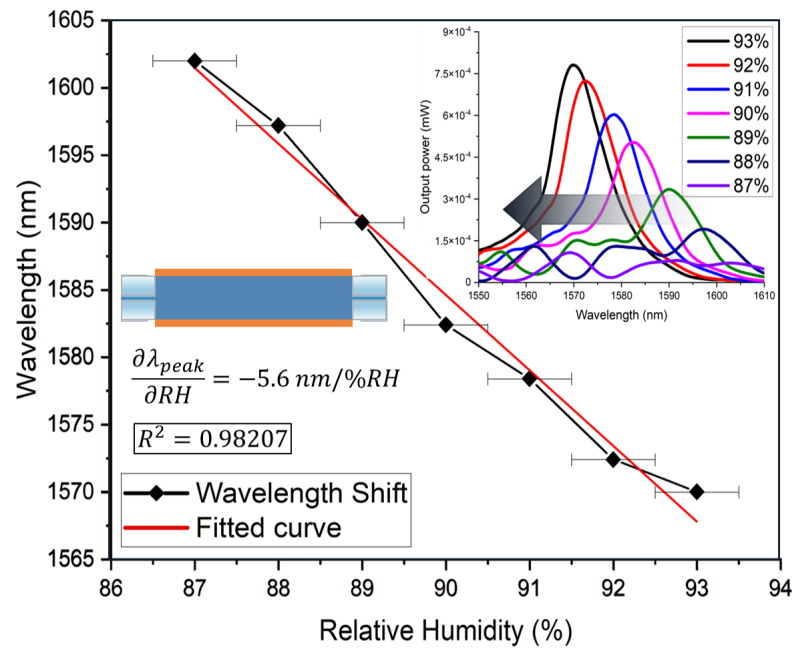


Figure 3. Transmission spectrum of an untapered PVA-coated NCF MMI device of $L = 59 \text{ mm}$ at RH of 87–93% showing a tuning range of 1570–1603 nm. The horizontal error bars indicate the resolution of the commercial hygrometer used in the experiments.

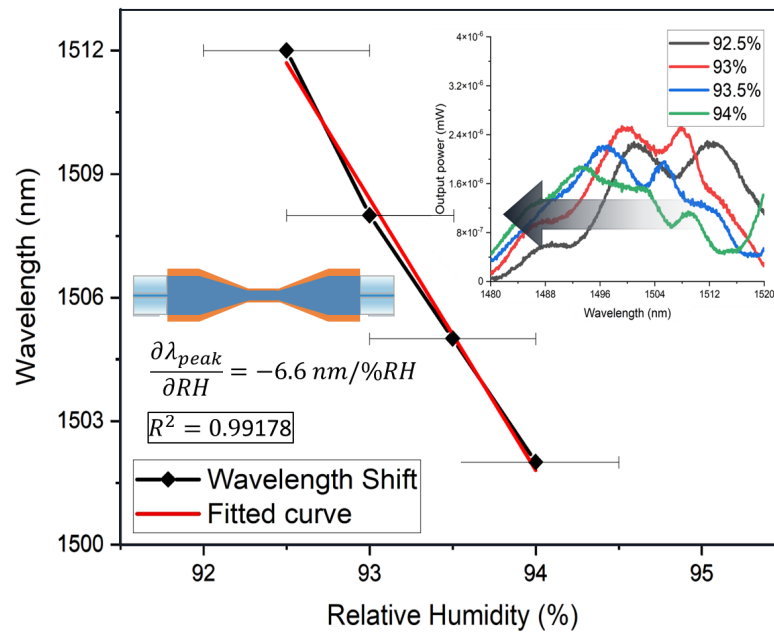


Figure 4. Transmission spectrum of a tapered PVA-coated NCF MMI device of $L = 59 \text{ mm}$ at RH of 92.5–94% showing a tuning range of 1502–1512 nm. The horizontal error bars indicate the resolution of the commercial hygrometer used in the experiments.

In the range of our experiments, the RI of PVA changes as a function of humidity at a rate of $3.3 \times 10^{-3} \text{ RIU}/(\%RH)$ [25]. This means that in the experiments with the native, non-tapered MMI sensor, the RI changed around 2×10^{-2} across the experiments, and the total wavelength shift was about 32.5 nm, which makes the sensitivity of $-5.6 \text{ nm}/(\%RH)$ to be equivalent to a refractometric sensitivity of $1.65 \times 10^3 \text{ nm}/\text{RIU}$, approximately. For the tapered MMI sensor, the RI changed around 5×10^{-3} across the experiments, and the total wavelength shift was about 10.5 nm, which makes the sensitivity of $-6.6 \text{ nm}/(\%RH)$ to be equivalent to a refractometric sensitivity of $2.10 \times 10^3 \text{ nm}/\text{RIU}$, approximately, representing

almost a 30% increase in sensitivity with respect to the native structure. The transmission spectra were recorded with a 0.08 nm resolution, such that the minimum RH variation that could be detected is 1.4×10^{-2} %RH and 1.2×10^{-2} %RH for the native and tapered structures, respectively.

Finally, Table 1 compares our sensor with the RH sensors reported in the literature over the last ten years, to the best of our knowledge, that are based on an MMI fiber structure. We included several characteristics i.e., structure, coating material, modifications to the structure, sensitivity, and sensing range, to have a more complete overview. The sensors presented in this work demonstrated high sensitivity to RH although their operation seems to be restricted to a narrow dynamic range. This behavior fits the trend with other cited high-sensitivity RH sensors with a shortened sensing range [26–28]. Moreover, the taper of the sensor presented is significantly thicker and shorter than those required in other works [27,29], which ultimately favors its manageability and robustness in practical applications.

Table 1. Comparison of RH sensors using MMI fiber structures.

Year	Structure	Material	Fiber Structure Novelty	Sensitivity	Sensing Range	Ref.
2013	SMF-MMF-SMF	PVA	Etched MMF (no cladding)	0.09 nm/%RH	30–80%	[21]
2014	SMF-MMF-SMF	PVS	Bitapers	0.139 nm/%RH	35–85%	[28]
2016	SMF-TSNCF-SMF	SiO ₂	TSNCF	0.5842 nm/%RH	83–96.6%	[26]
2017	SMF-NCF-SMF	AGF	NCF	0.149 nm/%RH	30–75%	[30]
2017	D-shaped fiber grating	Au-PVA	Surface plasmon D-fiber	0.54 nm/%RH	0–70%	[9]
2017	SMF-PCF-SMF	PAH-PAA	Photonic crystal fiber	2.35 nm/%RH	75–95%	[22]
2017	SMF-MMF(polished)-SMF	Gelatin	D-shape	0.14 dB/%RH	40–90%	[31]
2018	SMF-MMF(polished)-SMF	None	Fiber roughness	0.069 dB/%RH	30–90%	[32]
2018	SMF-Thin Core	PVA C	Rounded tip	0.4573 dB/%RH	>70%	[33]
2018	D-shaped SMF	PVA	Surface plasmon D-fiber	4.97 nm/%RH	80–90%	[34]
2019	SMF-NCF-SMF	GQD	Offset splice	0.421 dB/%RH	38.8–88.65%	[35]
2020	SMF-NCF-SMF	Al ₂ O ₃ PVA	Etched NCF	0.587 nm/%RH	30–100%	[10]
2020	Laser-SMF(Tapered)	Spider silk	Wrapped spider silk	0.789 nm/%RH	70–89%	[27]
2021	SMF(Tapered)	GO-PVA	Tapered SMF	0.529 %RH	20–99.9%	[29]
2023	SMF-NCF-SMF	PVA	NCF	5.6 nm/%RH	87–93%	*
2023	SMF-NCF-SMF	PVA	Tapered NCF	6.6 nm/%RH	92.5–94%	*

* Current work.

In the following, we analyze in more detail the performance of the sensor presented, starting with its dynamic range. The dispersion curve for neat PVA can be described with good approximation with a Cauchy dispersion model of the form $n = A + B\lambda^{-2}$, with the coefficients A and B having average values of 1.49 and $6.5 \times 10^{-3} \mu\text{m}^2$, respectively, and the wavelength λ given in microns [24,36–38]. At the wavelengths of interest, around 1550 nm, PVA has a RI of around 1.493, which is higher than the RI of the NCF (1.444). Therefore, at the baseline conditions (dry PVA), total internal reflection does not take place at the core/cladding interface in the multimode section of the MMI sensor; this, in turn, results in the coated NCF not being in a wave-guiding regime, but the light leaks out from it through the higher-RI PVA cladding, and no signal is measured. PVA exhibits a negative hygro-optic response, which means that its RI decreases as a function of water content. Several reports agree that the RI of PVA decreases approximately from 1.49 to 1.35 ($\Delta n \approx -0.14$) when humidity increases from 20%RH to 95%RH [25,39–43]. A closer look reveals that the RI of PVA depends nonlinearly on RH, but their relationship can be described as two linear regions: in the range from 20%RH to 74%RH, the RI of PVA decreases from 1.49 to about 1.42; and in the range from 74%RH to 98%RH, the RI of PVA decreases from 1.42 to about 1.34 [25]. Thus, with a simple PVA coating, our MMI sensor requires humidity to be around 70%RH for the NCF to start guiding the light. In practice, higher humidity is required to be able to measure a transmission spectrum, around 87%RH (see Figure 3). Extending the operation range of our sensor requires lowering the RI of the coating for the wave-guiding regime to be preserved at lower humidity values. That could be achieved

either by changing the coating material or by means of a PVA-based composite doped with a low-RI material.

Regarding the influence of the ambient temperature, it should be first noted that the definition of relative humidity is given at a constant temperature. Because of this, we kept the temperature invariant in the experiments. Although thermal effects were not tested experimentally, they can be estimated as follows. Strictly, a temperature change will affect both the dimensions of the optical fiber (thermal expansion of silica) and the refractive index (RI) of the materials (thermo-optic effects on silica and PVA). Regarding the thermal expansion of the NCF, fused silica has a very low expansion coefficient, on the order of $\alpha \approx 0.5 \times 10^{-6} \text{ }^\circ\text{C}^{-1}$; this makes the relative change of a linear dimension (length or diameter), ΔL , with respect to the original length, L_0 , to be minimal even for a large temperature change, ΔT , i.e., $\delta L/L_0 = \alpha \Delta T$. More specifically, by performing a simple variational analysis of Equation (1), the change in λ_{peak} produced solely by the thermal expansion of the NCF is $\Delta \lambda_{peak} = p n_{eff} (D_{eff} + \Delta D_{eff})^2 / (L + \Delta L) - \lambda_{peak,0}$, where $\Delta D_{eff} = \alpha \Delta T D_{eff,0}$, $\Delta L = \alpha \Delta T L_0$, and the subscript zero indicates the baseline condition. From this expression, it can be estimated that a change in the temperature of $\Delta T = 1 \text{ }^\circ\text{C}$ will produce a red shift of the transmitted spectrum of only $\Delta \lambda_{peak} \approx +7 \times 10^{-4} \text{ nm}$. Regarding the thermo-optic effects on the NCF, at around room temperatures, fused silica has a thermo-optic coefficient (TOC) on the order of $1 \times 10^{-5} \text{ }^\circ\text{C}^{-1}$ both in bulk [44] and optical fibers [45,46]. This indicates that the RI of the NCF varies only in the fifth decimal for small temperature variations. By performing a similar variational analysis of Equation (1), the change in λ_{peak} produced solely by thermo-optic effect on the NCF, is $\Delta \lambda_{peak} = p \Delta n_{eff} (D_{eff}^2) / L$, where $\Delta n_{eff} = \text{TOC} \times \Delta T$. From this expression, it can be estimated that a change in the temperature of $\Delta T = 1 \text{ }^\circ\text{C}$ will produce a red shift of $\Delta \lambda_{peak} \approx +1 \times 10^{-2} \text{ nm}$. Finally, PVA has a TOC of around $-2 \times 10^{-4} \text{ }^\circ\text{C}^{-1}$ [36,37]. These thermo-optic effects will reflect on the RI of the surrounding medium, n_m , and, consequently, on n_{eff} . To evaluate these effects, we follow the formalism presented in Ref. [47], where analytical expressions are provided to calculate n_{eff} explicitly as a function of n_m . By carrying out the calculations for the lowest order modes, which are most energetic ones, it can be estimated that a change in the temperature of $\Delta T = 1 \text{ }^\circ\text{C}$ will produce a negative change in n_{eff} smaller than 1×10^{-7} , which translates into a blue shift of $\Delta \lambda_{peak} \approx -1 \times 10^{-4} \text{ nm}$. In conclusion, thermal effects are negligible in our experiments; the dominant effect in the sensor's response is the change in the RI of PVA due to the absorption of water.

4. Conclusions

This work presented two RH sensors using a tapered and non-tapered NCF demonstrating outstanding sensitivities of 6.6 nm/RH% and 5.6 nm/RH% respectively. As predicted through theoretical examination, the sensitivity was experimentally demonstrated to increase by reducing the NCF fiber diameter through fusion splicer tapering. Even though the sensing range is far from desired, we believe short-RH-range sensors with high sensitivities could be suitable for several applications, especially those where humidity needs to be maintained around a target value. In this regard, we should remind the reader that we coated our MMI sensor with plain PVA; the sensitivity and dynamic range can be adjusted by using more sophisticated coatings. The merit of the present work is that a high sensitivity was achieved with a simple coating and commercial-grade optical fibers as well as the geometry of the taper allows preserving the mechanical robustness of the fiber structure. Also, the methods used to build the fiber structures offered high repeatability while also being relatively simple, inexpensive to build, and customizable. Ultimately, the combination of better materials and different taper geometries could lead to optimal performance, in terms of both the sensitivity and the dynamic range, for specific applications.

Author Contributions: Conceptualization and methodology: A.A.Q.-F., A.A.C.-G., and J.R.G.-S.; experiments, data collection, and data curation: A.A.Q.-F.; formal analysis: A.A.Q.-F., A.A.C.-G., and J.R.G.-S.; project supervision: A.A.C.-G. and J.R.G.-S. All authors contributed to writing the paper. All authors have read and agreed to the published version of the manuscript.

Funding: This research received no funding.

Institutional Review Board Statement: Not applicable.

Informed Consent Statement: Not applicable.

Data Availability Statement: Data underlying the results presented in this paper are not publicly available at this time but may be obtained from the corresponding author upon reasonable request.

Acknowledgments: A.A.Q.-F. acknowledges the Mexican National Council of Humanities, Science and Technology (CONAHCYT) for its support through a doctoral scholarship.

Conflicts of Interest: The authors declare that they have no known competing financial interest or personal relationships that could have appeared to influence the work reported in this paper.

Sample Availability: Not applicable.

References

1. Kersey, A.D. A review of recent developments in fiber optic sensor technology. *Opt. Fiber Technol.* **1996**, *2*, 291–317. [[CrossRef](#)]
2. Yin, S.; Ruffin, P.B.; Francis, T. *Fiber Optic Sensors*; CRC Press: Boca Raton, FL, USA, 2017.
3. Lee, C.Y.; Lee, G.B. Humidity sensors: A review. *Sens. Lett.* **2005**, *3*, 1–15. [[CrossRef](#)]
4. Farahani, H.; Wagiran, R.; Hamidon, M.N. Humidity sensors principle, mechanism, and fabrication technologies: a comprehensive review. *Sensors* **2014**, *14*, 7881–7939. [[CrossRef](#)] [[PubMed](#)]
5. Chen, Z.; Lu, C. Humidity sensors: A review of materials and mechanisms. *Sens. Lett.* **2005**, *3*, 274–295. [[CrossRef](#)]
6. Rao, X.; Zhao, L.; Xu, L.; Wang, Y.; Liu, K.; Wang, Y.; Chen, G.Y.; Liu, T.; Wang, Y. Review of optical humidity sensors. *Sensors* **2021**, *21*, 8049. [[CrossRef](#)]
7. Ascorbe, J.; Corres, J.M.; Arregui, F.J.; Matias, I.R. Recent developments in fiber optics humidity sensors. *Sensors* **2017**, *17*, 893. [[CrossRef](#)]
8. Patil, Y.H.; Ghosh, A. Optical fiber humidity sensors: A review. In Proceedings of the 2020 4th International Conference on Trends in Electronics and Informatics (ICOEI)(48184), Tirunelveli, India, 15–17 June 2020; pp. 207–213.
9. Yan, H.; Han, D.; Li, M.; Lin, B. Relative humidity sensor based on surface plasmon resonance of D-shaped fiber with polyvinyl alcohol embedding Au grating. *J. Nanophotonics* **2017**, *11*, 016008. [[CrossRef](#)]
10. Zebian, H.Y.; Taher, H.J. Relative humidity sensor based on no-core multimode interferometer coated with Al₂O₃-PVA composite films. *Opt. Fiber Technol.* **2020**, *54*, 102110. [[CrossRef](#)]
11. Kieu, K.Q.; Mansuripur, M. Biconical fiber taper sensors. *IEEE Photonics Technol. Lett.* **2006**, *18*, 2239–2241. [[CrossRef](#)]
12. Liu, H.; Miao, Y.; Liu, B.; Lin, W.; Zhang, H.; Song, B.; Huang, M.; Lin, L. Relative humidity sensor based on S-taper fiber coated with SiO₂ nanoparticles. *IEEE Sens. J.* **2015**, *15*, 3424–3428. [[CrossRef](#)]
13. André, R.M.; Biazoli, C.R.; Silva, S.O.; Marques, M.B.; Cordeiro, C.M.; Frazão, O. Strain-temperature discrimination using multimode interference in tapered fiber. *IEEE Photonics Technol. Lett.* **2012**, *25*, 155–158. [[CrossRef](#)]
14. Zhou, G.; Wu, Q.; Kumar, R.; Ng, W.P.; Liu, H.; Niu, L.; Lalam, N.; Yuan, X.; Semenova, Y.; Farrell, G.; et al. High sensitivity refractometer based on reflective SMF-small diameter no core fiber structure. *Sensors* **2017**, *17*, 1415. [[CrossRef](#)] [[PubMed](#)]
15. Guzmán-Sepúlveda, J.R.; Guzmán-Cabrera, R.; Castillo-Guzmán, A.A. Optical sensing using fiber-optic multimode interference devices: A review of nonconventional sensing schemes. *Sensors* **2021**, *21*, 1862. [[CrossRef](#)]
16. Wu, Q.; Qu, Y.; Liu, J.; Yuan, J.; Wan, S.P.; Wu, T.; He, X.D.; Liu, B.; Liu, D.; Ma, Y.; et al. Singlemode-multimode-singlemode fiber structures for sensing applications—A review. *IEEE Sens. J.* **2020**, *21*, 12734–12751. [[CrossRef](#)]
17. Wang, K.; Dong, X.; Köhler, M.H.; Kienle, P.; Bian, Q.; Jakobi, M.; Koch, A.W. Advances in optical fiber sensors based on multimode interference (MMI): A review. *IEEE Sens. J.* **2020**, *21*, 132–142. [[CrossRef](#)]
18. Zhao, Y.; Zhao, J.; Zhao, Q. Review of no-core optical fiber sensor and applications. *Sens. Actuators A Phys.* **2020**, *313*, 112160. [[CrossRef](#)]
19. Wang, P.; Zhao, H.; Wang, X.; Farrell, G.; Brambilla, G. A review of multimode interference in tapered optical fibers and related applications. *Sensors* **2018**, *18*, 858. [[CrossRef](#)]
20. Guzman-Sepulveda, J.R.; Castillo-Guzman, A.A. Wavelength Tuning of Multimode Interference Fiber Lasers: A Review. *Adv. Photonics Res.* **2021**, *2*, 2100051. [[CrossRef](#)]
21. An, J.; Zhao, Y.; Jin, Y.; Shen, C. Relative humidity sensor based on SMS fiber structure with polyvinyl alcohol coating. *Optik* **2013**, *124*, 6178–6181. [[CrossRef](#)]
22. Lopez-Torres, D.; Elosua, C.; Villatoro, J.; Zubia, J.; Rothhardt, M.; Schuster, K.; Arregui, F.J. Photonic crystal fiber interferometer coated with a PAH/PAA nanolayer as humidity sensor. *Sens. Actuators B Chem.* **2017**, *242*, 1065–1072. [[CrossRef](#)]

23. Fuentes-Rubio, Y.A.; Domínguez-Cruz, R.F.; Guzmán-Sepúlveda, J.R. Multipoint fiber optics refractive index sensor based on multimode interference effects. *Appl. Opt.* **2021**, *60*, 9691–9695. [[CrossRef](#)] [[PubMed](#)]
24. Schnepf, M.J.; Mayer, M.; Kuttner, C.; Tebbe, M.; Wolf, D.; Dulle, M.; Altantzis, T.; Formanek, P.; Förster, S.; Bals, S.; et al. Nanorattles with tailored electric field enhancement. *Nanoscale* **2017**, *9*, 9376–9385. [[CrossRef](#)]
25. Miao, Y.; Liu, B.; Zhang, H.; Li, Y.; Zhou, H.; Sun, H.; Zhang, W.; Zhao, Q. Relative humidity sensor based on tilted fiber Bragg grating with polyvinyl alcohol coating. *IEEE Photonics Technol. Lett.* **2009**, *21*, 441–443. [[CrossRef](#)]
26. Miao, Y.; Ma, X.; He, Y.; Zhang, H.; Zhang, H.; Song, B.; Liu, B.; Yao, J. Low-temperature-sensitive relative humidity sensor based on tapered square no-core fiber coated with SiO₂ nanoparticles. *Opt. Fiber Technol.* **2016**, *29*, 59–64. [[CrossRef](#)]
27. Liu, Z.; Zhang, M.; Zhang, Y.; Xu, Y.; Zhang, Y.; Yang, X.; Zhang, J.; Yang, J.; Yuan, L. Spider silk-based tapered optical fiber for humidity sensing based on multimode interference. *Sens. Actuators A Phys.* **2020**, *313*, 112179. [[CrossRef](#)]
28. An, J.; Jin, Y.; Sun, M.; Dong, X. Relative humidity sensor based on SMS fiber structure with two waist-enlarged tapers. *IEEE Sens. J.* **2014**, *14*, 2683–2686. [[CrossRef](#)]
29. Syuhada, A.; Shamsudin, M.S.; Daud, S.; Krishnan, G.; Harun, S.W.; Aziz, M.S.A. Single-mode modified tapered fiber structure functionalized with GO-PVA composite layer for relative humidity sensing. *Photonic Sens.* **2021**, *11*, 314–324. [[CrossRef](#)]
30. Xu, W.; Shi, J.; Yang, X.; Xu, D.; Rong, F.; Zhao, J.; Yao, J. Relative humidity sensor based on no-core fiber coated by agarose-gel film. *Sensors* **2017**, *17*, 2353. [[CrossRef](#)]
31. Wang, X.; Farrell, G.; Lewis, E.; Tian, K.; Yuan, L.; Wang, P. A humidity sensor based on a singlemode-side polished multimode-singlemode optical fibre structure coated with gelatin. *J. Light. Technol.* **2017**, *35*, 4087–4094. [[CrossRef](#)]
32. Wang, X.; Tian, K.; Yuan, L.; Lewis, E.; Farrell, G.; Wang, P. A high-temperature humidity sensor based on a singlemode-side polished multimode-singlemode fiber structure. *J. Light. Technol.* **2018**, *36*, 2730–2736. [[CrossRef](#)]
33. Ma, Q.F.; Tou, Z.Q.; Ni, K.; Lim, Y.Y.; Lin, Y.F.; Wang, Y.R.; Zhou, M.H.; Shi, F.F.; Niu, L.; Dong, X.Y.; et al. Carbon-nanotube/Polyvinyl alcohol coated thin core fiber sensor for humidity measurement. *Sens. Actuators B Chem.* **2018**, *257*, 800–806. [[CrossRef](#)]
34. Shao, Y.; Wang, Y.; Cao, S.; Huang, Y.; Zhang, L.; Zhang, F.; Liao, C.; Wang, Y. Mechanism and characteristics of humidity sensing with polyvinyl alcohol-coated fiber surface plasmon resonance sensor. *Sensors* **2018**, *18*, 2029. [[CrossRef](#)] [[PubMed](#)]
35. Tong, R.j.; Zhao, Y.; Chen, M.q.; Peng, Y. Multimode interferometer based on no-core fiber with QDs-PVA composite coating for relative humidity sensing. *Opt. Fiber Technol.* **2019**, *48*, 242–247. [[CrossRef](#)]
36. Doudou, B.B.; Jaouadi, H.; Dridi, C. Prism coupling technique investigation of optical and thermo-optical properties of polyvinyl alcohol and polyvinyl alcohol/silica nanocomposite films. *Opt. Commun.* **2021**, *492*, 126984. [[CrossRef](#)]
37. Doudou, B.B.; Chiba, I.; Daoues, H.S. Optical and thermo-optical properties of polyvinyl alcohol/carbon nanotubes composites investigated by prism coupling technique. *Opt. Mater.* **2022**, *131*, 112672. [[CrossRef](#)]
38. Ko, B.; Badloe, T.; Yang, Y.; Park, J.; Kim, J.; Jeong, H.; Jung, C.; Rho, J. Tunable metasurfaces via the humidity responsive swelling of single-step imprinted polyvinyl alcohol nanostructures. *Nat. Commun.* **2022**, *13*, 6256. [[CrossRef](#)]
39. Gastón, A.; Pérez, F.; Sevilla, J. Optical fiber relative-humidity sensor with polyvinyl alcohol film. *Appl. Opt.* **2004**, *43*, 4127–4132. [[CrossRef](#)] [[PubMed](#)]
40. Dong, X.; Li, T.; Liu, Y.; Li, Y.; Zhao, C.L.; Chan, C.C. Polyvinyl alcohol-coated hybrid fiber grating for relative humidity sensing. *J. Biomed. Opt.* **2011**, *16*, 077001. [[CrossRef](#)]
41. Li, T.; Dong, X.; Chan, C.C.; Zhao, C.L.; Zu, P. Humidity sensor based on a multimode-fiber taper coated with polyvinyl alcohol interacting with a fiber Bragg grating. *IEEE Sens. J.* **2011**, *12*, 2205–2208. [[CrossRef](#)]
42. Yang, J.; Dong, X.; Ni, K.; Chan, C.C.; Shun, P.P. Intensity-modulated relative humidity sensing with polyvinyl alcohol coating and optical fiber gratings. *Appl. Opt.* **2015**, *54*, 2620–2624. [[CrossRef](#)]
43. Hsieh, M.C.; Liao, C.H.; Lin, J.Y. Optical relative humidity sensor based on a polyvinyl alcohol film and a phase-enhancement total-internal-reflection heterodyne interferometer. *Sens. Actuators A Phys.* **2020**, *316*, 112412. [[CrossRef](#)]
44. Palik, E.D. *Handbook of Optical Constants of Solids*; Academic Press: Cambridge, MA, USA, 1998; Volume 3.
45. Chang, S.; Hsu, C.C.; Huang, T.H.; Chuang, W.C.; Tsai, Y.S.; Shieh, J.Y.; Leung, C.Y. Heterodyne interferometric measurement of the thermo-optic coefficient of single mode fiber. *Chin. J. Phys.* **2000**, *38*, 437–442.
46. Gao, H.; Jiang, Y.; Cui, Y.; Zhang, L.; Jia, J.; Jiang, L. Investigation on the thermo-optic coefficient of silica fiber within a wide temperature range. *J. Light. Technol.* **2018**, *36*, 5881–5886. [[CrossRef](#)]
47. Xu, W.; Shi, J.; Yang, X.; Xu, D.; Rong, F.; Zhao, J.; Yao, J. Improved numerical calculation of the single-mode-no-core-single-mode fiber structure using the fields far from cutoff approximation. *Sensors* **2017**, *17*, 2240. [[CrossRef](#)] [[PubMed](#)]

Disclaimer/Publisher’s Note: The statements, opinions and data contained in all publications are solely those of the individual author(s) and contributor(s) and not of MDPI and/or the editor(s). MDPI and/or the editor(s) disclaim responsibility for any injury to people or property resulting from any ideas, methods, instructions or products referred to in the content.